PAPER Nr. : 5

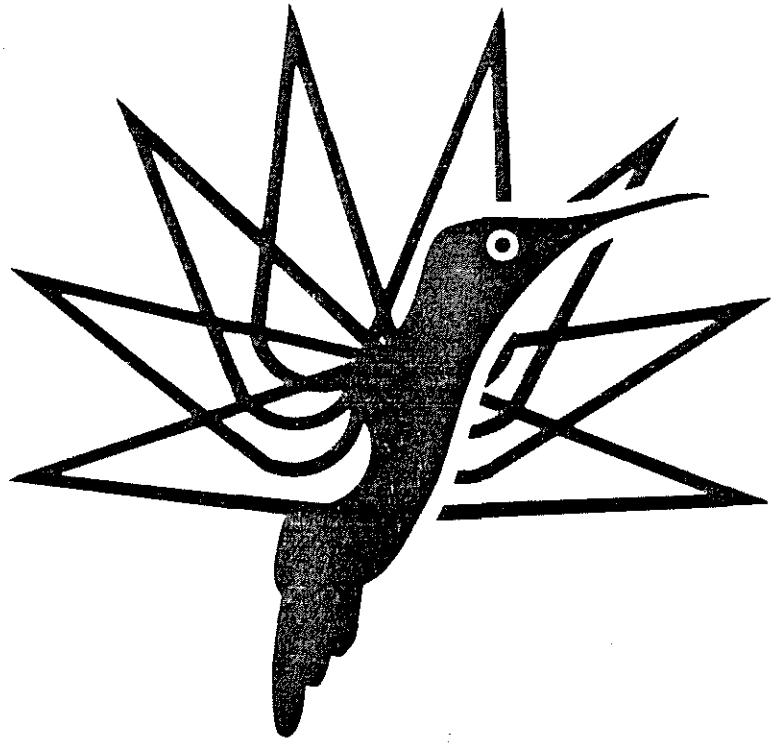

EXPERIMENTAL AND NUMERICAL STUDY OF THE FLOW AROUND AN HELICOPTER FUSELAGE. DETERMINATION OF DRAG COEFFICIENT.

BY

C. GLEYZES - X de SAINT-VICTOR
ONERA/CERT TOULOUSE (FRANCE)

G. FALEMPIN
ONERA CHATILLON (FRANCE)

FIFTEENTH EUROPEAN ROTORCRAFT FORUM

SEPTEMBER 12 - 15, 1989 AMSTERDAM

EXPERIMENTAL AND NUMERICAL STUDY OF THE FLOW AROUND AN HELICOPTER FUSELAGE. DETERMINATION OF DRAG COEFFICIENT.

C. GLEYZES - X. de SAINT-VICTOR
ONERA-CERT, TOULOUSE (FRANCE)
G. FALEMPIN
ONERA, CHATILLON (FRANCE)

Abstract

This paper presents the contribution of ONERA to a better understanding and prevision of the flow around helicopter fuselages. Besides a detailed experimental study of a simple geometry, efforts have been done for the validation and improvements of codes, and a low computing time procedure has been developed, based on a weak viscous–inviscid interaction, between a 3D boundary layer integral method and a potential flow calculation including a prescribed rigid geometry wake. For geometries where large separated areas are not present, this code provides realistic estimation of the aerodynamic forces on the body.

1 Introduction :

In order to improve the prevision of the flow around helicopter fuselages, a cooperation between ONERA and AEROSPATIALE has been undertaken on three major axes :

- detailed experimental study of a simplified fuselage geometry ;
- validation of 3D boundary layer and potential flow calculation codes ;
- developpement of a procedure able to estimate aerodynamic forces on the fuselage.

First part of this study has been reported previously [9] so that we will just remind here some main results, and present new developements. We will then discuss about drag coefficient computations, with some application results.

2 Previous studies :

2.1 Experiments :

They have been conducted on a simplified geometry fuselage, in the F2 wind tunnel, which is specially devoted to research programs [1]. This wind tunnel is

fitted with a 3D LDV system, which has been widely used to provide detailed experimental results in two characteristic configurations :

$$\alpha = 0^o \text{ and } \alpha = -5^o \text{ , for } U_\infty = 40ms^{-1}$$

Boundary layer surveys at around 40 locations on the model provided useful comparisons with calculation method, while wake surveys gave very helpful results for the understanding of the flow patterns.

Besides these LDV measurements, oil flow visualizations and wall pressure measurements were performed.

2.2 Boundary layer calculations :

The method we use [6,7,8] deals with three–dimensional boundary layer integral equations written in a general surface coordinate system. Starting from given initial conditions (generally provided by stagnation point solutions) and knowing the metrics of the coordinate system (obtained by geometric transformations), integration of the equations proceeds by X-marching and needs the data of boundary conditions.

These conditions consist in magnitude (U_e) and direction (ψ) of inviscid velocity at the edge of the boundary layer, and were taken, at this stage, from inviscid flow calculations without wake.

An important preliminary comment was that for all test conditions, oil flow visualizations show the presence of a laminar separation bubble at the beginning of the constant section part of the body [9]. If this bubble caused a natural transition (checked by transition visualizations), it was however very large, and we had to estimate the overthickening of the bubble all around the body in order to have reasonable agreement at the first measuring station. This was of course only possible for $\alpha = 0$ and -5^o where boundary layer measurements were available.

3 Extension of boundary layer calculations :

As in the first half of the body, agreement between measured and computed wall pressure is good (see, for instance, figure 2), we can expect a satisfactory behaviour of boundary layer calculations in this region, using inviscid pressure field. When approaching separated region, at the rear of the body, discrepancies arise on the pressure field, and boundary layer calculations lead to erroneous results. Consequently, for this model, additionnal calculations have been done with the velocity field deduced from experiments. For the determination of these boundary conditions, a procedure was extended from a code previously developed [10], to solve Euler equations, using the experimental pressure field in the rear part of the model, starting from theoretical initial conditions at the middle of the model.

Figure 1 presents, for $\alpha = 0^o$, an example of results obtained on the lateral mid line ($\varphi = 90^o$) compared with the experimental results, using both theoretical and experimental pressure fields. Agreement is quite satisfactory, for both calculations, up to the beginning of the aft contraction ($x = 525mm$),

but the use of experimental pressure field strongly improves agreement on the downstream rapid growth on boundary layer thickness.

Let us now examine figure 2 showing the evolutions of skin friction coefficient along the lower symmetry line of the model, for $\alpha = 0^o$. Here, separation is similar to a base flow one. Calculation using potential (without wake) and experimental pressure fields have been plotted. One could expect that the experimental pressure field would be the ideal result for a potential flow calculation including correct modelling of the wake. Effectively, we can note that upstream of separation, agreement is significantly improved. But, because boundary layer calculation is performed in direct mode, we find a behaviour related to the well–known singularity at a 2D separation. In this case, the calculation reaches the constant pressure area before the adverse pressure gradient induces separation.

We can see there some aspect of the limitations of a weak viscous–inviscid interaction technique for configurations where large quasi–2D separations exist.

4 Calculation of friction drag :

4.1 Equations :

If we consider a point P on the surface, the coordinates of which are $x^{1'}$, $x^{2'}$, $x^{3'}$ in cartesian system (base vectors $\overrightarrow{e_{1'}}$, $\overrightarrow{e_{2'}}$, $\overrightarrow{e_{3'}}$), and X^1, X^2 in a general coordinate system (base vectors $\overrightarrow{a_1}$, $\overrightarrow{a_2}$) defined on the surface, we can then write [12] :

$$x^{i'}\ \overrightarrow{e_{i'}} = X^\alpha\ \overrightarrow{a_\alpha} \text{ for } i' = 1,3 \quad \alpha = 1,2$$

We deduce :

$$\overrightarrow{a_\alpha} = \overrightarrow{e_{i'}}\ \beta_\alpha^{i'} \text{ where } \beta_\alpha^{i'} = \frac{\partial x^{i'}}{\partial X^\alpha}$$

Note that the surface system is completed by the normal X^3, which has a unit base vector $\overrightarrow{a_3}$.

Tensor $\beta_j^{i'}$ so obtained provides the metric tensor on the surface :

$$a_{\alpha\beta} = \sum_{k'=1}^{3} \beta_\alpha^{k'}\ \beta_\beta^{k'} \text{ for } \alpha,\ \beta = 1,2$$

Note that usual metric elements needed for boundary layer calculations are often written as :

$$h_1 = \sqrt{a_{11}},\ h_2 = \sqrt{a_{22}} \text{ and } \lambda = \arccos \frac{a_{12}}{h_1\ h_2}$$

We compute then projections dF_s et dF_n , in a streamline coordinate system (related to local external flow direction) of the local friction force applied on surface ds surrounding the grid point ($ds = \sqrt{a_{11}\ a_{22} - {a_{12}}^2}\ dX^1\ dX^2$), knowing local skin friction C_f and its direction β_0 relative to external velocity U_e, using :

$$dF_s = \frac{1}{2}\rho_e {U_e}^2 C_f \, ds \, \cos\beta_0$$

$$dF_n = \frac{1}{2}\rho_e {U_e}^2 C_f \, ds \, \sin\beta_0$$

Contravariant components dF^1 and dF^2 (dF^3 being 0 by definition) in the general surface cordinate system are then given by :

$$dF^1 = \frac{\left(dF_s \sin(\lambda - \psi) - dF_n \cos(\lambda - \psi)\right)}{h_1 \sin\lambda}$$

$$dF^2 = \frac{\left(dF_s \sin\psi + dF_n \cos\psi\right)}{h_2 \sin\lambda}$$

After projection in the cartesian coordinate system :

$$dF^{i'} = \sum_{\alpha=1}^{2} dF^{\alpha} \beta_{\alpha}^{i'} \quad , \; i' = 1,3$$

the integration on all the body provides global viscous aerodynamic forces.

4.2 Application to the F2 model :

From boundary layer calculation results previously performed without as well as with the effects of the separation bubble, using potential flow pressure distributions [9], computations of viscous drag forces have been done, for $\alpha = 0^o$ and $\alpha = -5^o$, and have been compared to balance drag measurements performed by AEROSPATIALE [5].

On the other hand, the wake surveys were used to look at the vortical drag of the body. According to previous studies [16,11], we can deduce it from the following integral :

$$Rx_t = \int\int_S \frac{1}{2}\rho\,(V^2 + W^2)\,ds$$

where S is the front section of the wind tunnel, downstream of the model.

Figures 3 and 4 show the plots of the secondary velocities (V, W) measured in the wake for $\alpha = 0^o$ and $\alpha = -5^o$. A rough estimation of this vortical drag was then given by an integration performed on the measurement domain limited by the symmetry plane. Although measurements are available only in the lower part of the wake of the model, the quantity $(V^2 + W^2)$ is almost vanishing at the boundaries of the measurement domain, except near the tail boom, where LDV measurement could not be performed close enough to the wall. Consequently, results are probably under–estimated, but we can reasonably admit that the differences between the two incidences are significant of the change in the pattern of the wake.

The table below collects the results so obtained (drag coefficients based on the maximum cross–section of the body) :

α (degree)	friction drag computed without bubble	friction drag computed with bubble	vortical drag estimated from wake survey	total drag measured (balance)
0	0.040	0.054	0.032	0.125
-5	0.040	0.054	0.078	0.210

A first comment is that the viscous drag do not depend on incidence, and that the influence of the overthickenning due to the laminar bubble is far from negligible. For $\alpha = 0°$, the pressure drag corresponds to around 57% of the total drag, while for $\alpha = -5°$, this figure goes up to 75%. If we look then to the estimations of the vortical drag, we confirm here that the change in the structure of the wake we had seen between the two incidences [9] leads to an important increase in drag, by a factor of more than 2.5 as, mainly for $\alpha = -5°$, most of the vorticity is concentrated along the tail boom, part of it in an inaccessible area for LDV measurements.

We can also notice that when adding friction and vortical drags, we do not reach the value of the total drag. This is probably due partly in the under–estimation of the vortical wake, partly in the fact that all the pressure drag is not induced by the vorticity of the wake.

5 Viscous–inviscid interaction :

5.1 Equations :

Definition of displacement thickness or transpiration velocity is related to the idea of viscous–inviscid interaction. The main relation allowing for the matching of these two flows concerns the velocity component normal to the wall. This is achieved by combining the global continuity equation written in the boundary layer, and an extension towards the wall of the inviscid flow, deduced from local continuity equation written for inviscid flow [14]. If we define the following quantities :

- $U_1 = U_e \frac{\sin(\lambda-\psi)}{\sin\lambda}$, edge velocity in the direction X^1 ;
- $W_1 = U_e \frac{\sin\psi}{\sin\lambda}$, edge velocity in the direction X^2 ;
- $q = h_1\, h_2 \sin\lambda$, metric element ;
- Δ_1 , displacement thickness in the direction X^1 ;
- Δ_2 , displacement thickness in the direction X^2 ;

we can for instance, compute the displacement thickness δ^* defined by Lighthill [15], using the following partial differencial equation :

$$\frac{\partial}{\partial X^1}\left[\frac{\rho_e q}{h_1}(\delta^* U_1 - \Delta_1 U_e)\right] + \frac{\partial}{\partial X^2}\left[\frac{\rho_e q}{h_2}(\delta^* W_1 - \Delta_2 U_e)\right] = 0$$

The matching condition for the viscous–inviscid interaction can be done at any distance X^3 from the wall, but is usually written at $X^3 = 0$, for numerical reasons, and corresponds to a transpiration condition at the wall, given by :

$$\frac{V_0^*}{U_e} = \frac{1}{\rho_e U_e q}\frac{\partial}{\partial X^1}\left(\frac{\rho_e U_e q \Delta_1}{h_1}\right) + \frac{1}{\rho_e U_e q}\frac{\partial}{\partial X^2}\left(\frac{\rho_e U_e q \Delta_2}{h_2}\right)$$

Starting from a first potential flow calculation around the body without wake, a first boundary layer calculation provides then a new set of wall boundary conditions for the inviscid flow ($\vec{V} \,.\, \vec{n} = V_0^*$). These conditions are then introduced in a new potential flow calculation. For large separated areas, this new calculation takes into account a rigid prescribed geometry wake [13], the origin of which being the separation line indicated by the boundary layer calculation. For small separated areas, this type of modelling of the wake is not used because of numerical problems (see 5-3), and a simple potential flow calculation code without wake is used. In both cases, the new pressure field obtained after some iterations should provide the pressure drag of the model, while boundary layer calculation results should provide friction drag. We will present some examples in the following sections.

5.2 Application to the F2 model :

Figure 5 gives a map of the displacement thickness computed on the F2 model, from the first boundary layer calculation. One can see the separated area, at the aft contraction, where no boundary layer calculation was available.

For this configuration, various computations have been performed. Figure 6 shows the corresponding pressure distributions, compared with experimental results. Case (1) corresponds to the basic initial result, from which boundary layer calculation have been performed. Case (2) corresponds to the same potential code, in which transpiration velocities have been taken into account (note the slight discontinuity, at the separation line, due to the lack of transpiration velocity results downstream of separation). For these two cases, wake is not taken into account. For case (3), a wake originated at the separation line given by the boundary layer calculation has been taken into account, with the classical slip condition, while in case (4) transpiration velocities have been added.

If we compare results (1-2) and (3-4), we can note that the viscous–inviscid interaction gives good tendencies, that is to say a decrease of the second suction peak, but the changes are very limited to this area. In addition, these effects are small and we are still far away from experiments. Comparing results (1-3), it is obvious that the presence of the wake has much larger effects. In particular, the changes on the pressure field are extending much more upwards,

and seem to give a much better agreement with experiments, at least upstream of separation. Introduction of transpiration velocities (calculation 4) slightly improves agreement on the second suction peak. Unfortunately, the level of the pressure downstream of the separation line is poorly predicted.

As the computed separation was located downstream of the experimental one (see Fig. 7), additionnal calculations were performed, with four different locations of the line on which the wake is initiated. Figure 8 gives the pressure distributions along a meridian line, compared with the experimental one. For this type of geometry, we can see that the results are very dependent on the location of the separated line (see Fig. 7). However, results obtained in case (1), corresponding to the separation line indicated by the boundary layer calculation seem to give the best agreement with experiments, upstream of separation. Unfortunately, the downstream nearly constant pressure level is not well predicted, leading to errors in pressure drag. For case (4), corresponding to a wake initiated on a line close to the experimental separation line, agreement is very poor upstream of separation, and if the pressure level downstream of separation is closer to the experimental one, it is still too high. For the four cases, the adverse pressure gradient upstream of the separation is too large, leading, for calculation case (1) in particular, to a separation line moving upwards when trying to go into the iterative procedure. As a consequence, we have not been able to give any estimation of the pressure drag, as it is directly function of the pressure level on the aft contraction.

If one had not been yet convinced of the importance of vortical drag, this shows obviously that improvements in the wake modelling are strongly needed.

5.3 Application to GARTEUR model :

As we have seen previously, this simple procedure is, at the present stage, not well suited for geometries where massive separation exists. Fortunately, this kind of fuselage geometry is not really adapted to high performances, and a tool able to minimize the drag of a fuselage, mainly by optimizing the shapes, and able, in these conditions to give correct estimation of aerodynamic coefficients, at low cost, can be helpful for pre–design steps.

In this prospect, this procedure has been applied to a more streamline geometry tested at DLR in the framework of a GARTEUR action group [3].

Calculations were then performed for angles of attack $\alpha = 0^o$,-2.5^o and -5^o, for $U_\infty = 60\, ms^{-1}$, with a natural transition corresponding to a turbulence level of 0.10% [4]. Figures 9, 10 and 11 give rear views at the first iteration, of the computed wall streamlines for the three incidences, and show the increase with incidence of the separated area. We can however note that the flow pattern seems to be unchanged : for all cases, the three–dimensional separation at the round lower edge of the aft contraction induces a weak vortical wake, which is confirmed by the wake surveys [2]. This behaviour indicates that, for this range of incidence, no drastic change in drag is expected. We can also note that this fuselage presents separated areas much smaller than the F2 model.

The transpiration velocity obtained from the three–dimensional bound-

ary layer calculation have then been introduced in inviscid flow calculation code. Calculations with wake were first attempted, but because of the shape of the body, interaction between singularities on the wake and on the aft contraction was important, and convergence of the method could not be achieved. Here also, improvements in the wake modelling are needed. However, as the effects of the wake seems to be weak, we performed then calculations without wake.

Because it was not possible to reproduce the experimental sting support, the geometry was closed by a conical end, giving a residual pressure drag due to the discontinuity. Consequently, pressure drag was obtained by substraction from the results after iterations, of the non–zero pressure drag obtained at the initialisation.

On figure 12 are plotted the evolutions with iterations of the two components of drag. We can see that for pressure drag, convergence is obtained within 4 to 5 iterations, with some oscillations. Some relaxation should probably help in reducing this number.

Figures 13 and 14 show the pressure contours on the aft contraction at initial and final stages of the iterative process, for $\alpha = -5°$. We can note that on most of the body, pressure fields are very similar, except at the lower part of it, where wall streamlines converge and generate the vortical separation. In this area, pressure field is strongly distorted, and most of the pressure drag is produced there.

For the friction drag, the influence of the transpiration velocities is quite negligible, as convergence was obtained after very few iterations. In fact, separation is very three–dimensional and is induced by transverse pressure gradients due to the geometry of the lower round edge of the aft contraction. Consequently, surface flow pattern and by the side skin friction distributions, are very little affected by the modifications of the pressure field which have only very small influence on these gradients. This can be seen on figure 16, where are plotted, for $\alpha = -5°$, the wall streamlines obtained after 5 iterations, which show very few differences with figure 15 which corresponds to the initial boundary layer results. Agreement with experimental results is also fairly good. In particular, the flow pattern in the nose region, showing a rapid change in wall shear stress direction associated with transition (Fig. 17) if fairly well predicted.

Table below gives the results we have obtained, compared with measurements performed at DFVLR (reference to $1\,m^2$).

α (degree)	friction drag (computed)	pressure drag (computed)	total drag (computed)	total drag balance
0	0.00400	0.0003	0.0043	0.0045
-2.5	0.00402	0.00112	0.00514	0.0052
-5.	0.00411	0.00181	0.00592	0.0060

We can first note that the viscous drag is slightly increasing with incidence, but much less than total drag. Second point is that, as expected for this configuration, the pressure drag is low, compared with the viscous one, but

increases with incidence, which is consistent with the increase of the size of separated area. Note that the friction drag coefficients are in reasonable good agreement with calculations performed by NLR and AEROSPATIALE [3], although boundary conditions are not obtained through the same codes (AEROSPATIALE uses a code with only sources, while ONERA uses sources and doublets, which usually gives better results).

Globally, we can see that the estimation of the total drag is in fairly good agreement with experimental results.

6 Conclusions :

The study of the flow around a simplified helicopter fuselage has been carried out, as part of cooperation between AEROSPATIALE (Helicopter Division) and ONERA.

First part of this work consisted in a detailed study of the model, in the F2 wind tunnel. Pressure measurements, visualizations and mainly three-dimensional LDV surveys provided a large amount of data.

On the other hand, comparisons with boundary layer calculations showed that simple inviscid flow calculations could provide boundary conditions giving reasonable overall agreement upstream of separation.

However, for this type of geometry, a good prediction of aerodynamic characteristics (mainly pressure drag), seems more difficult and should probably go through improvements in the modelling of the wake in inviscid flow calculation.

Fortunately, for more streamline geometries, the procedure we have developed provides, at reasonable cost, good estimation of the drag of the fuselage, and can be used for body shape optimization.

Acknowledgement

Financial support of this study has been provided by DRET, which is gratefully acknowledged.

References

[1] **D Afchain, P Broussaud, M Frugier, G Rancarani:** *"La soufflerie F2 du centre du Fauga-Mauzac"* presented at 20th AAAF meeting, november 1983.

[2] **S R Ahmed, J Amtsberg:** *"An experimental study of the aerodynamic characteristics of three helicopter fuselages"* presented at the XIII European Rotorcraft Forum, Arles, september 1987.

[3] **S R Ahmed, J Amtsberg, A De Bruin, A Cler, G Falempin, T H Le, G Poltz, F T Wilson:** *"Comparison with experiments of var-*

ious computational methods of airflow on three helicopter fuselages" presented at the XIV European Rotorcraft Forum, Milan, september 1988.

[4] **D Arnal, M Habiballah, E Coustols :** *"Théorie de l'instabilité laminaire et critères de transition en écoulements bi et tridimensionnels"* La Recherche Aérospatiale 1984-2.

[5] **A Cler:** *"Affinement fuselages - partie expérimentale"* AEROSPATIALE/DH, STPA/HE fiche 2/48, 1986.

[6] **J Cousteix:** *"Analyse théorique et moyen de prévision de la couche limite turbulente tridimensionnelle"* ESA translation TT 238

[7] **B Aupoix, J Cousteix :** *"Etude et développement d'une méthode intégrale de calcul des couches limites tridimensionnelles"* R.T. 8/3327 EY , 1980.

[8] **J Cousteix, C Gleyzes, B Aupoix:** *"Analysis of three-dimensional separation by using a boundary layer approach"* Int. Conf. on Fluid Mechanics, Beijing (China), july 1987.

[9] **C Gleyzes, X de Saint Victor, A Cler :** *"Experimental study of the flow around an helicopter fuselage. Comparison with three-dimensionnal boundary layer calculations."* presented at the XIV European Rotorcraft Forum, Milan, september 1988.

[10] **C Gleyzes, J Cousteix :** *"Calcul des lignes de courant à partir des pressions pariétales sur un corps fuselé."* La Recherche Aérospatiale 1984-3.

[11] **T H Halstaff, G W Brune :** *"An investigation of civil afterbody drag using a three-dimensional wake survey method."* AIAA paper No 84-0614 1984.

[12] **E h Hirschell, W Kordulla :** *"Shear flow in surface-oriented coordinates."* Notes on numerical fluid mechanics, Vol 4, Vieweg, 1981.

[13] **T H Le, J Ryan, G Falempin :** *"Wake modelling for helicopter fuselages.* presented at the XIII European Rotorcraft Forum, Arles, september 1987.

[14] **J C Le Balleur :** *"Couplage visqueux-non visqueux. Analyse du problème incluant décollements et ondes de choc."* La Recherche Aérospatiale 1977-6.

[15] **M J Lighthill :** *"On displacement thickness."* JFM 4, 1958.

[16] **E C Maskell :** *"Progress towards a method of measurements of the components of the drag of a wing of finite span."* RAE TP 72232 1973.

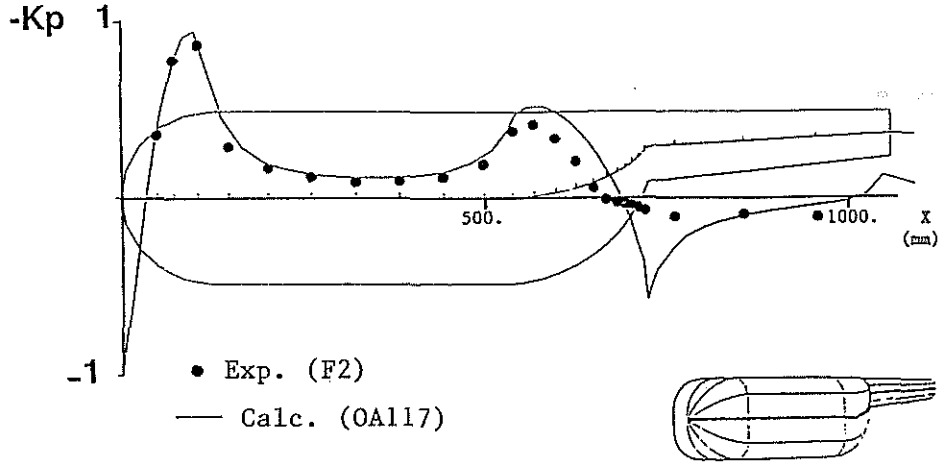

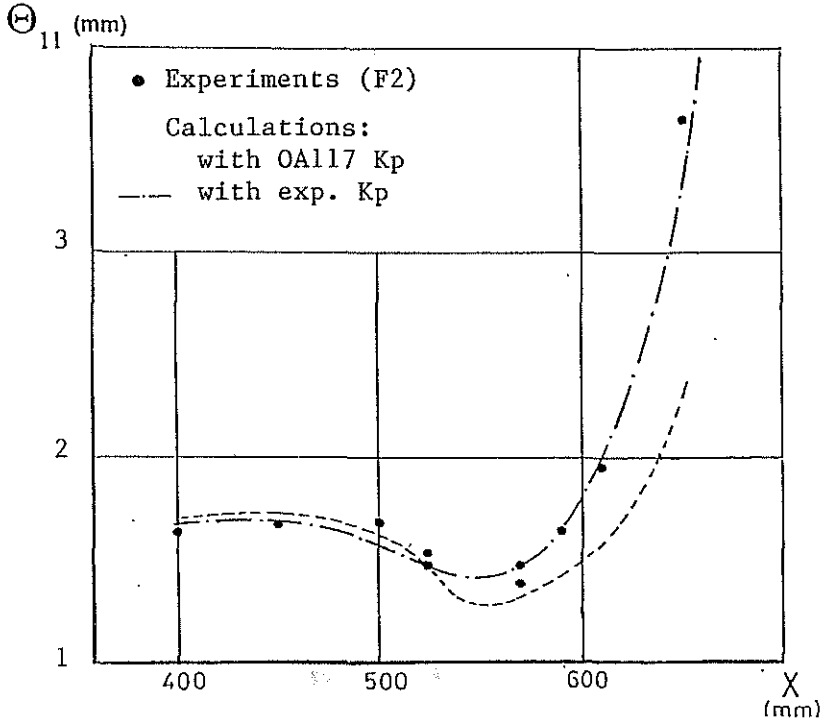

Fig. 1 Boundary layer calculations along lateral mid-line
$\alpha = 0°$. Influence of boundary conditions.

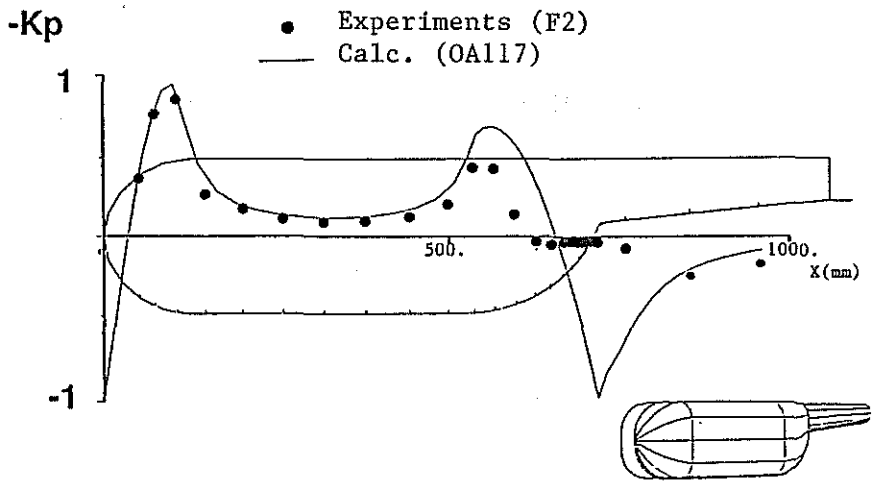

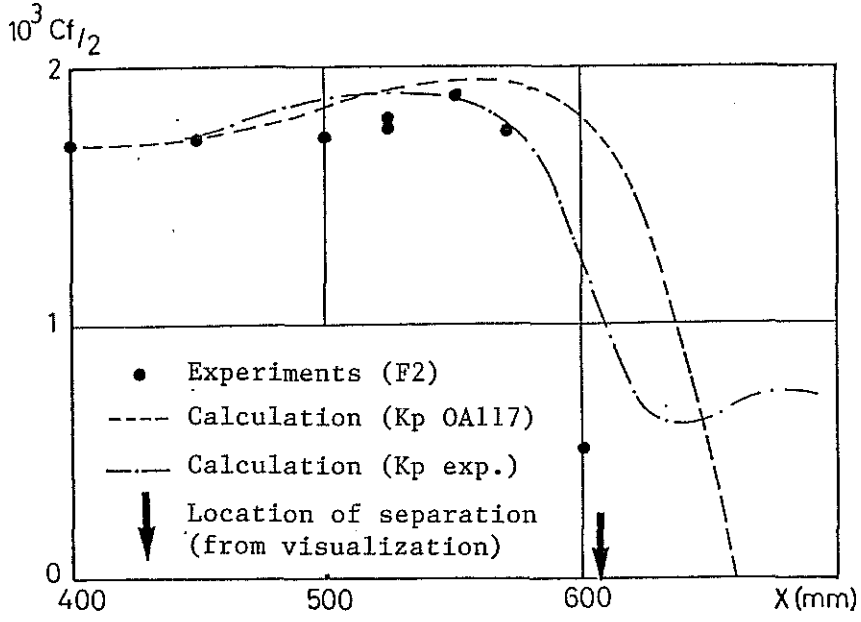

Fig. 2 Boundary layer calculations along lower symmetry line
$\alpha = 0°$. Influence of boundary conditions.

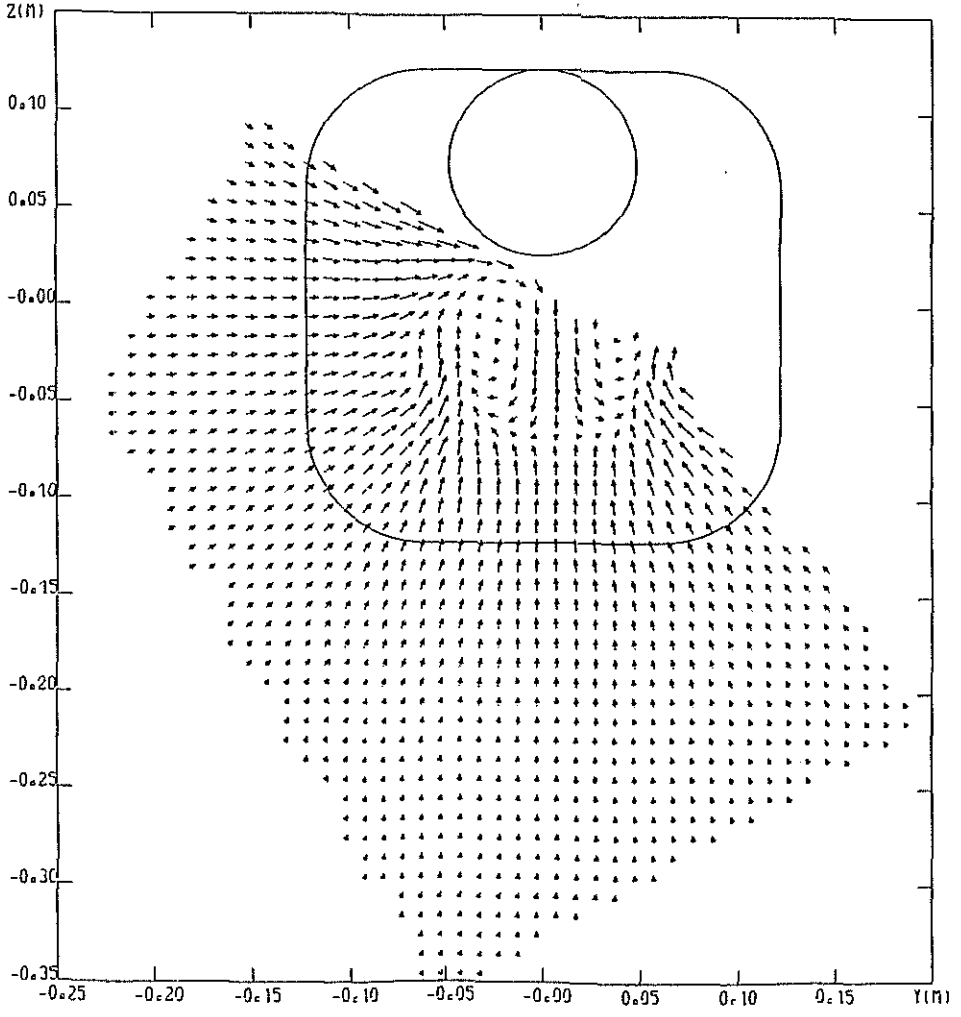

Fig. 3 Secondary velocities in the wake of the model . $\alpha = 0°$

$\sqrt{(V^2 + W^2)} = 0.5\ U_o$ →

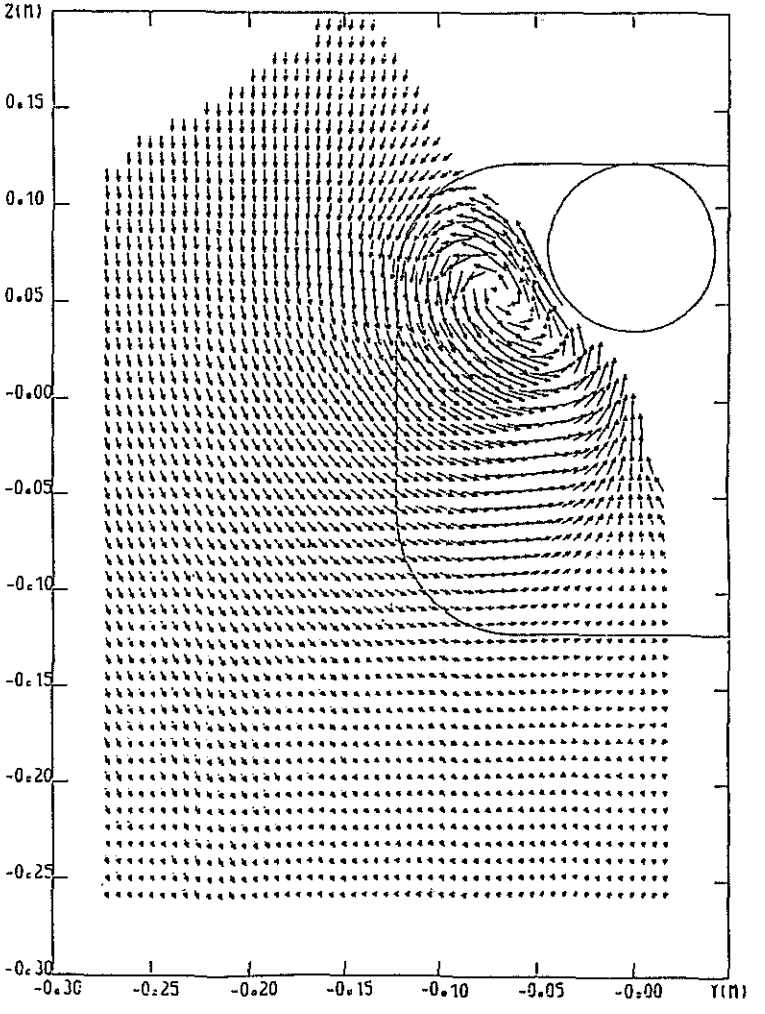

Fig. 4 Secondary velocities in the wake of the model . $\alpha = -5°$

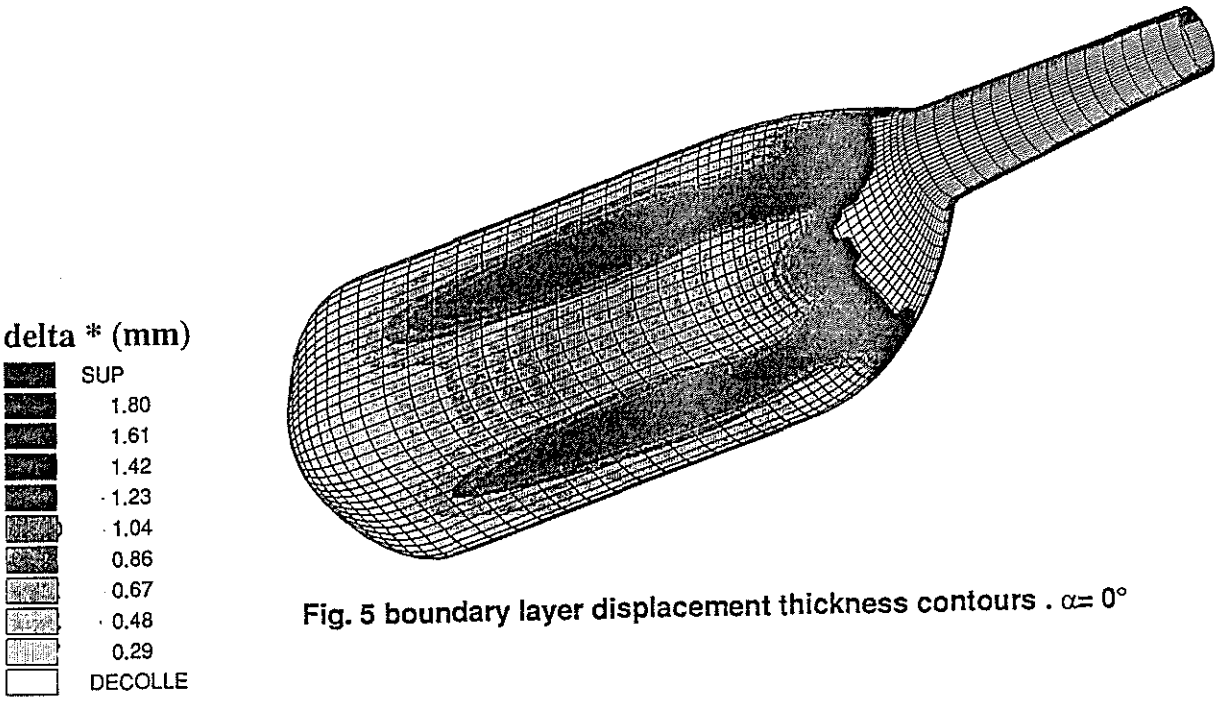

Fig. 5 boundary layer displacement thickness contours . $\alpha = 0°$

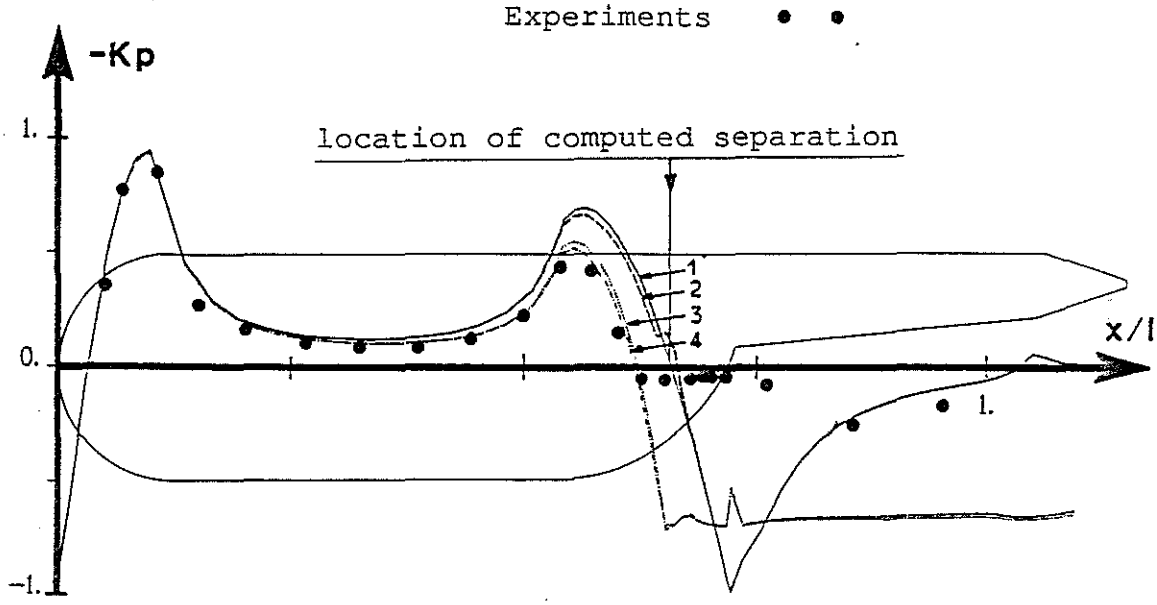

Fig. 6 Pressure distributions along lower symmetry line
$\alpha = 0°$. Influence of boundary conditions.

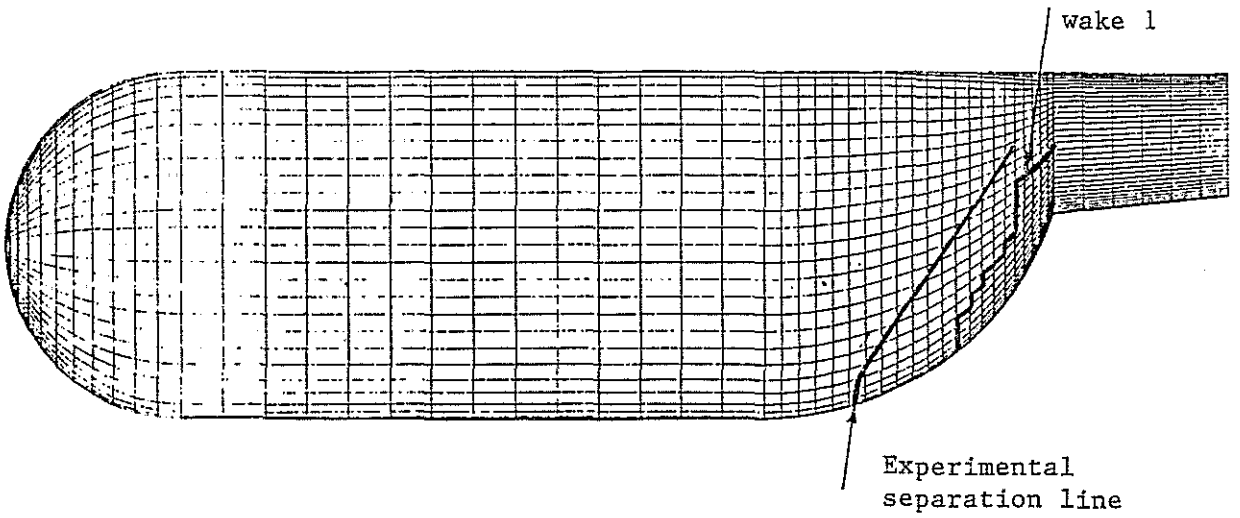

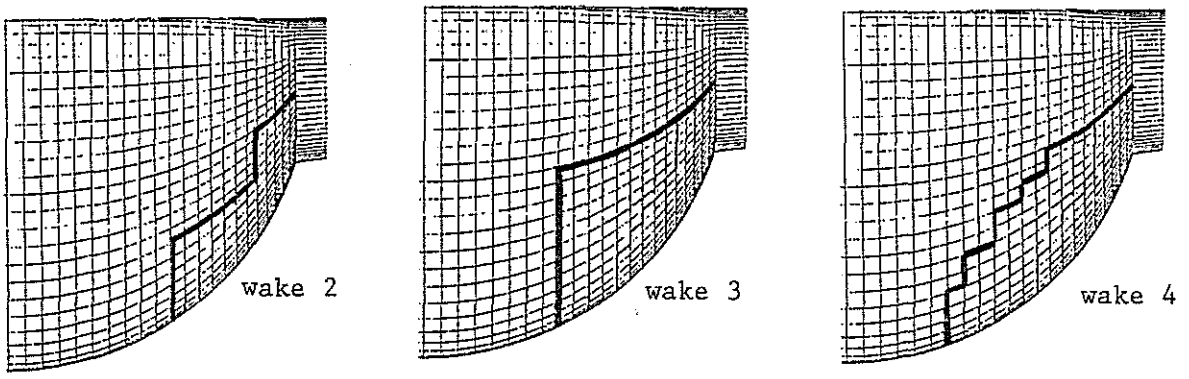

Fig. 7 Location of the various wake emission lines used in the computation tests. $\alpha = 0°$

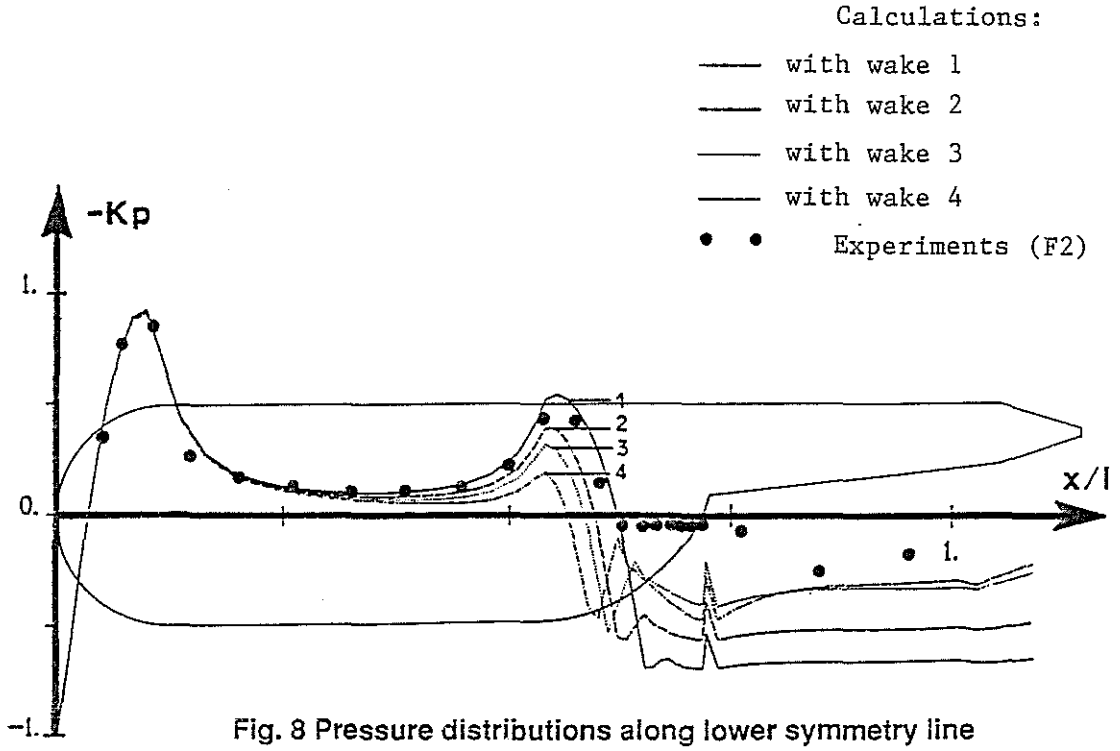

Fig. 8 Pressure distributions along lower symmetry line $\alpha = 0°$. Influence of location of separation line

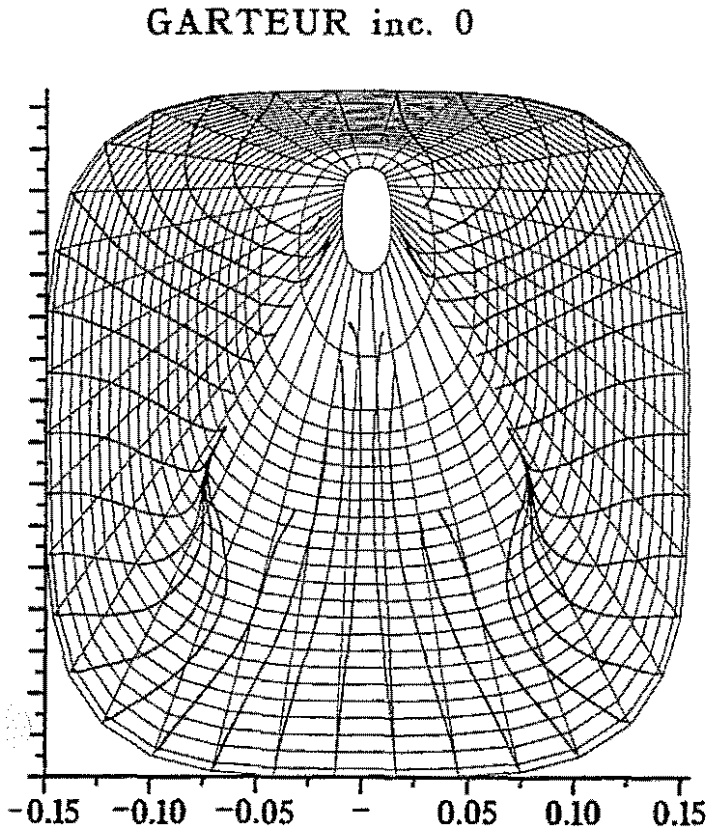

Fig. 9 Computed wall streamlines
on the GARTEUR model.Rear view. $\alpha = 0°$.

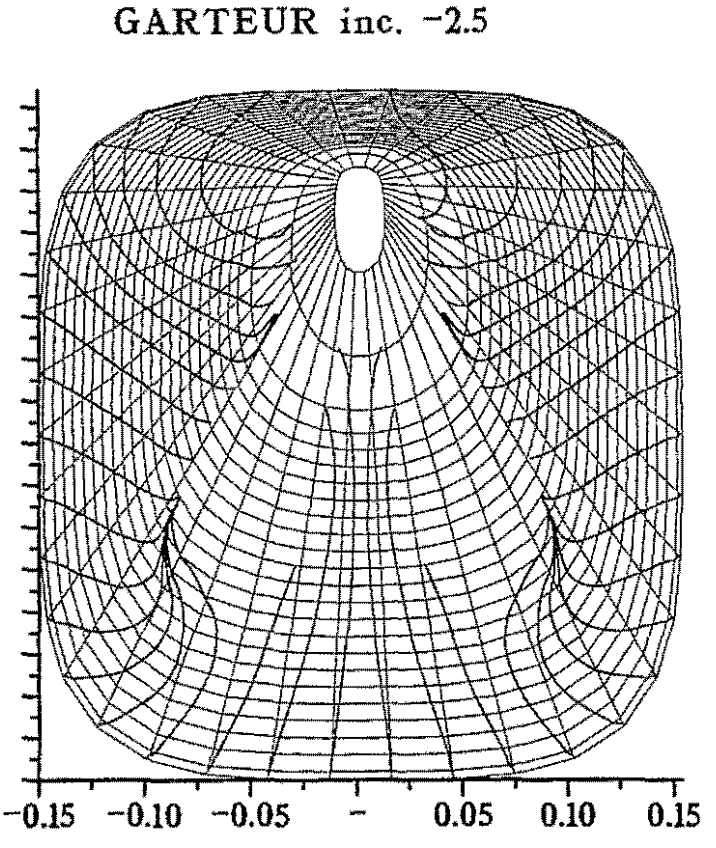

Fig. 10 Computed wall streamlines
on the GARTEUR model.Rear view. $\alpha = -2.5°$.

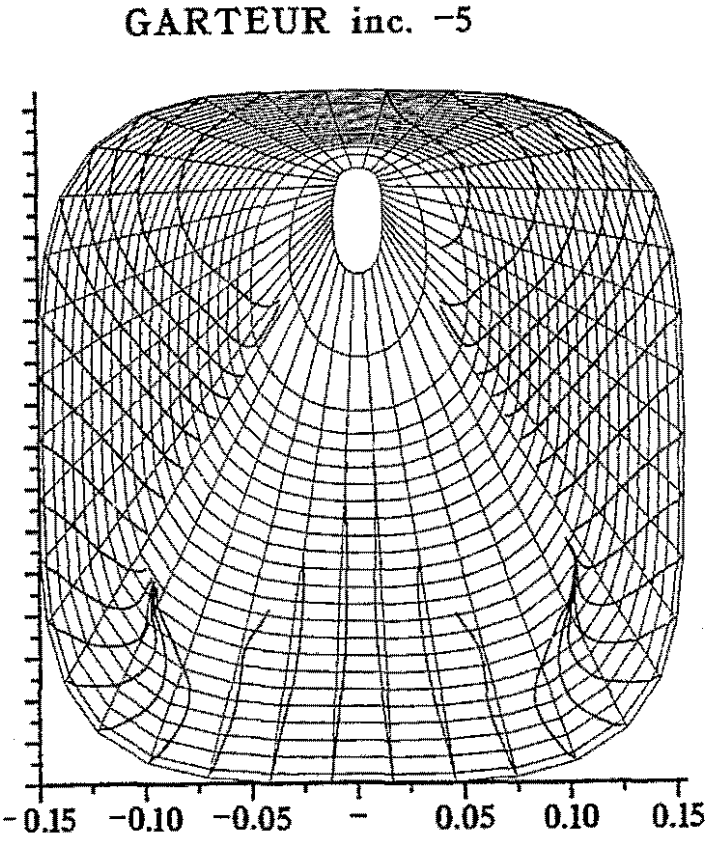

Fig. 11 Computed wall streamlines
on the GARTEUR model.Rear view. $\alpha = -5°$.

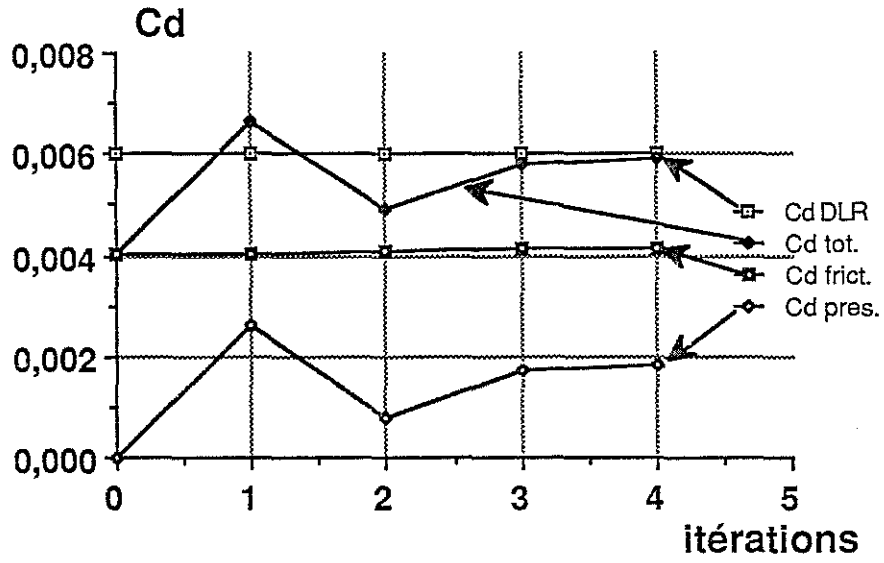

Fig. 12 Evolution of drag components with iterations. α= -5°.

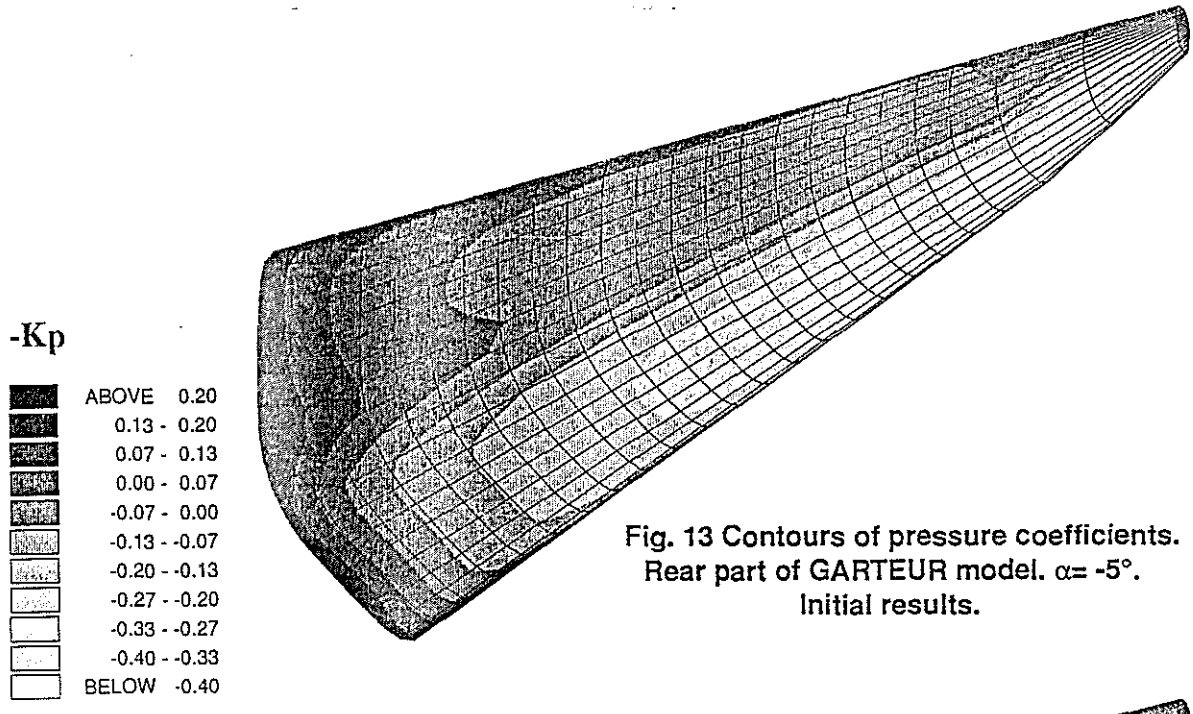

Fig. 13 Contours of pressure coefficients.
Rear part of GARTEUR model. α= -5°.
Initial results.

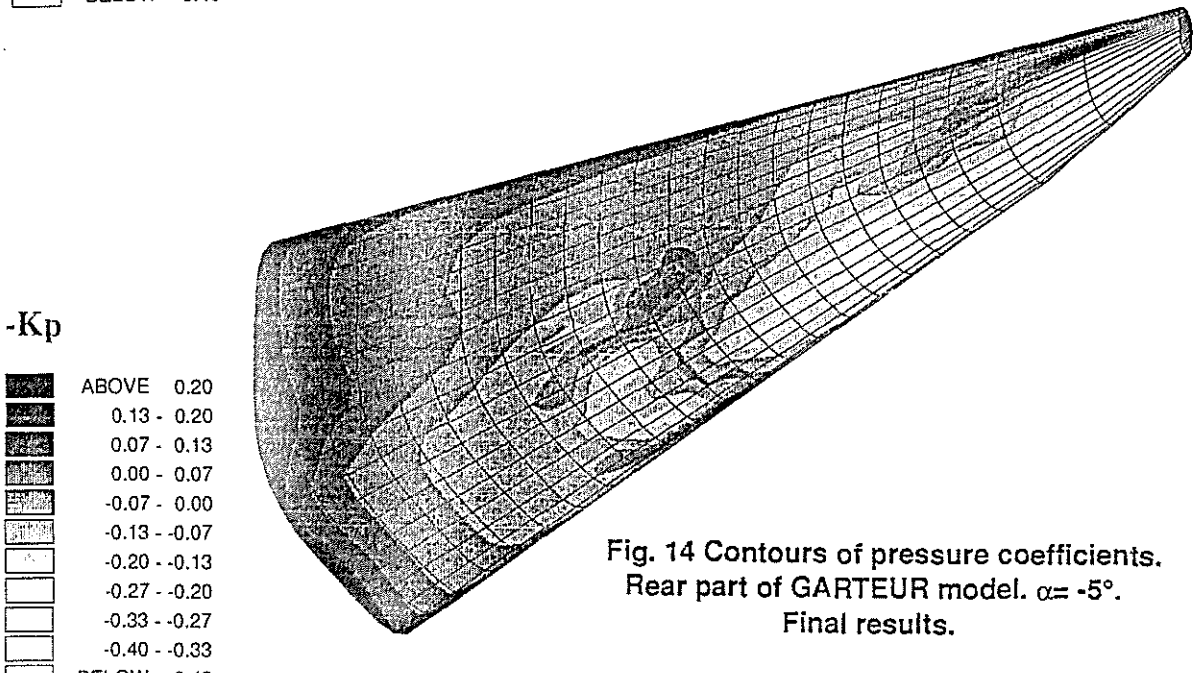

Fig. 14 Contours of pressure coefficients.
Rear part of GARTEUR model. α= -5°.
Final results.

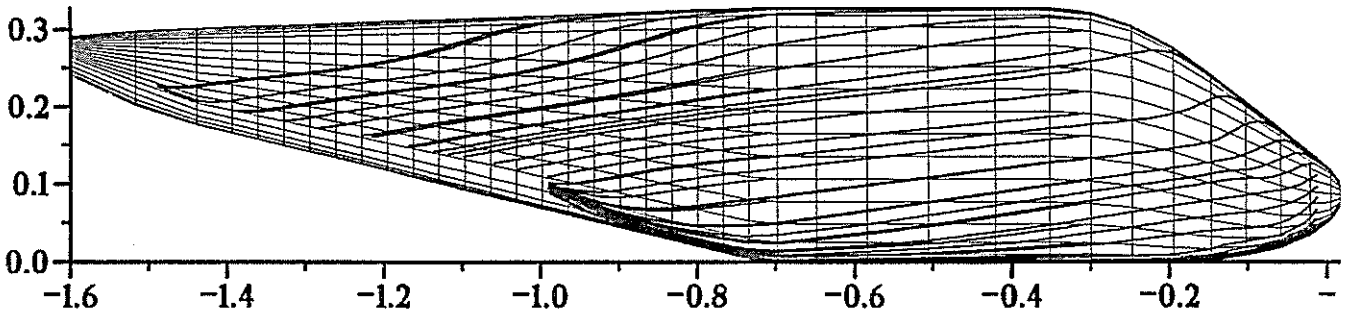

Fig. 15 Computed wall streamlines
on the GARTEUR model.Initial step. α = -5°.

Fig. 16 Computed wall streamlines
on the GARTEUR model.Final step. α = -5°.

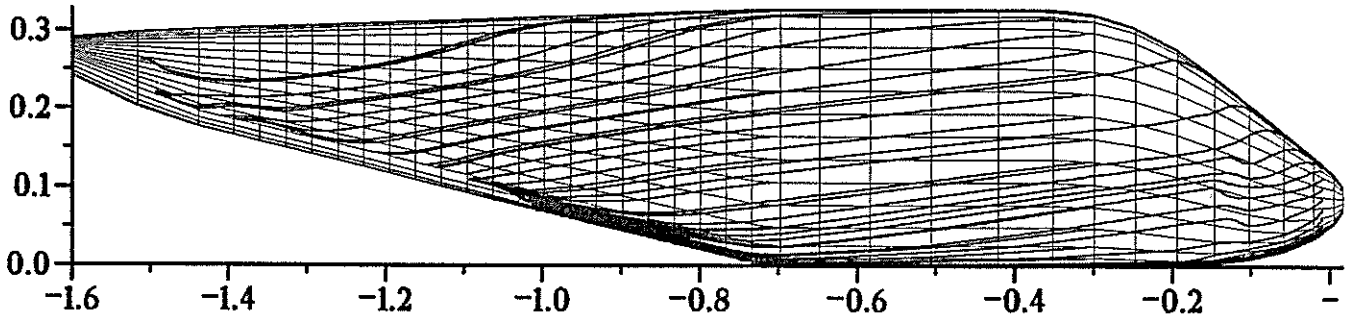

Fig. 17 Experimental wall streamlines
on the GARTEUR model.Nose region. α = -5°.
Courtesy of GARTEUR Group.